Magnetic Fields Induced by Electrochemical Reactions: Aluminum Alloy Corrosion Sensing by SQUID Magnetometry on a Macroscopic Scale

Yu Pei Ma,[†] **John P. Wikswo,**[†] **Meilutė Samulevičienė,**[‡] **Konstantinas Leinartas,**[‡] **and Eimutis Juzeliūnas*,**[‡]

Department of Physics and Astronomy, Vanderbilt University, VU Station B 351807, Nashville, Tennessee 37235, and Institute of Chemistry, A. Goštauto 9, 2600 Vilnius, Lithuania

Received: June 13, 2002

Corrosion of aluminum alloy AA 2024 at room temperature was studied in NaCl solutions by a SQUID magnetometer operating in liquid helium. Macroscopic electronic current flow along an asymmetric U-shaped sample was indicated by distinctive magnetic field images with a spatial resolution of the order of 1 mm. It was concluded that the macroscopic current originated from a corrosion potential gradient within the sample because of its asymmetric geometry; this current was negligible on an equipotential (symmetric) sample. Electrochemical quartz crystal microbalance measurement demonstrated that oxygen plays a significant part in this corrosion process, allowing control of corrosion activity of AA 2024 by changing the oxygen content in the solution. The asymmetric sample was magnetically sensitive to corrosion: the higher corrosion rate with increased oxygen concentration resulted in higher magnetic activity. By contrast, the sample that was a system of single sections did not produce a magnetic field that reflected increases in corrosion rate, and magnetic activity of this sample was much less than that of its monolithic counterpart. The obtained data demonstrated that a uniformly corroding surface could be magnetically silent on a macroscopic scale if no special measures are undertaken to distort the equipotentiality of the corroding surface.

1. Introduction

The detection of magnetic fields associated with electron and ion transfer at the electrode−electrolyte interface provides a new method for remote sensing of electrochemical processes. Such research is part of magnetoelectrochemistry, which deals with the magnetic fields induced by electrochemical reactions[1−16] or vice versa, the influence of magnetic fields upon electrochemical reactions.[17−31] Of these two areas, the corrosion of metals has the greatest practical significance. The major advantage of the magnetometric corrosion sensing lies in its ability to detect the corrosion activity across a dielectric medium. The magnetometric approach also provides a unique possibility of sensing subsurface or "hidden" corrosion or detecting of corrosion activity in restricted locations, as in the case of crevice, intergranular, or exfoliation corrosion.

The first attempts to use superconducting quantum interference device (SQUID) magnetometry to study the magnetic fields produced by metals exposed to electrolyte were reported in refs 1 and 2. These experiments were continued by other authors using a high-resolution scanning magnetometer-imaging system, which comprised five SQUIDs operating in liquid helium.[3]

The first SQUID magnetometer specifically designed for corrosion studies was reported by Hibbs and co-workers.[4] The equipment had a spatial resolution of the order of 1 mm with a sensitivity of 3 pT/Hz$^{1/2}$ (at 1 Hz). The detection coil array of this system was orientated at 45° with respect to the dewar axis. The design of the system allowed rotation of the dewar about

its axis, thereby changing the coil axis from vertical to horizontal. This made it possible to orient the corroding sample vertically and thereby avoid undesirable gas bubble accumulation on the surface.

Studies by Li et al. produced maps of the magnetic field distribution over aircraft aluminum alloy plates immersed in NaCl solution with Cu(II) additive.[5−7] The magnetic field was shown to be dependent upon the immersion time, chloride concentration, the distance between the SQUID detector and the sample, and the sample thickness. The ability of SQUID magnetometers to monitor electrochemical activity within components removed from actual aircraft has also been demonstrated.[8,9]

Recently, a SQUID magnetic imaging system was designed and built by Wikswo and co-workers at Vanderbilt University for high-resolution, long-term, and quantitative spatio-temporal imaging of hidden corrosion activity in planar aircraft structures.[10] The system consists of a three-axis differential magnetometer, magnetic shielding, a computer controlled x−y stage, sample registration and positioning mechanisms, and data acquisition and analysis software. It was capable of scanning samples with a spatial resolution of 2 mm and a sensitivity of 0.3 pT/Hz$^{1/2}$ (at 10 Hz).

SQUID magnetometry has been used to study corrosion of aluminum alloys in air, distilled water, and exfoliation test solution (ASSET).[11] Measurements were conducted in a nonmagnetic room by using a special wagon to move a sample immersed in solution. The distance between the sample and the bottom of the cryostat was 15 mm. The detected magnetic signal was ascribed to corrosion because it was not detected for samples in distilled water.

A high-T_c SQUID magnetometer operating in liquid nitrogen was used to study the correlation between magnetic fields and

* To whom correspondence should be addressed. E-mail: ejuzel@ktl.mii.lt.
† Vanderbilt University.
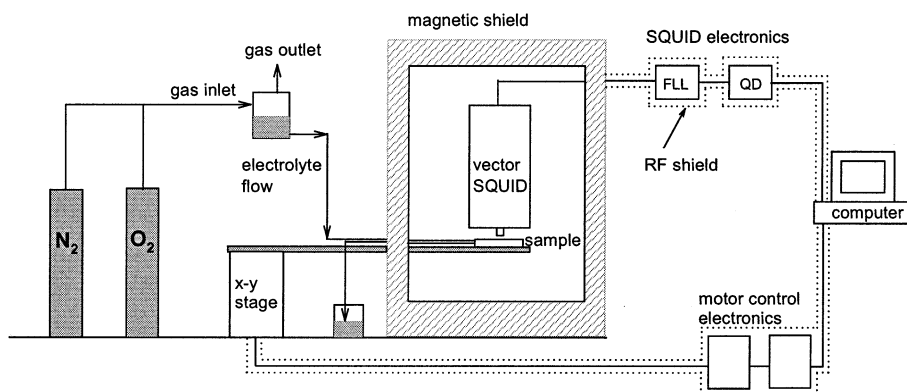‡ Institute of Chemistry.

Figure 1. Experimental setup of the magnetic imaging system. The system consists of a three-axis differential SQUID magnetometer, magnetic and rf shielding, and an $x-y$ stage.

the initiation of corrosion in Ni−Cr−Mo and Co−Cr−Mo alloys, which are used as metallic biomaterials.[12,13] The specimen was placed in a compartment filled with nitrogen gas and a hemispherical water layer was formed on the specimen. The SQUID detected magnetic fields when corrosion was initiated by supplying oxygen gas into the compartment.

It has been shown that the magnetic fields were generated both normal and parallel to the metal/liquid interface when liquid contacted the metal surface; provided both the phases were at different temperatures.[14] These results are important in SQUID interfacial studies where thermal equilibrium within the sample could be distorted, for instance at elevated temperatures or when exothermic reactions occur.

Abedi used appropriate experimental techniques and associated models in order to quantify the corrosion rate through measurements of associated magnetic field.[15] He defined quantitative magnetic parameters in conjunction with mass loss measurements and concluded that spatial and temporal information of corrosion magnetic fields correlates with that of corrosion currents.

It is commonly known that aluminum alloys corrode according to the so-called pitting mechanism, which includes breakdown of passivity, pit growth, and repassivation phenomena. The corrosion mechanism of an AA 2024 alloy, which was investigated in this paper, is discussed in detail in the literature.[32−39] The corrosion process consists of at least two coupled charge-transfer reactions, i.e., metal oxidation

$$Me \rightarrow Me^{z+} + ze \qquad (I)$$

and oxidizer reduction

$$Ox + ze \rightarrow Red^{z-} \qquad (II)$$

The first reaction is localized within the pit, whereas the second one may take place outside this domain. This means that electrons produced in reaction 1 flow within the metal from the metal ionization site to that of oxidizer reduction. Subsequent currents may originate from diffusion or/and migration of the Me^{z+} or Red^{z-} in the solution phase or the associated movement of other ionic species in the solution.

Detection of magnetic activity within a single corrosion pit would require a SQUID magnetometer with a sufficiently high spatial resolution (in order of micrometers), which has not yet been achieved for room temperature samples. A uniformly corroding surface could be magnetically silent on a macroscopic scale because of statistically distributed corrosion pits and randomly oriented surface currents and/or the unbroken translational symmetry of the corroding system. Thus, uniform

corrosion may not be detectable by using conventional SQUID scanning techniques, provided no special measures are undertaken to activate the surface on a macroscopic scale or break the symmetry of the system. Hence, we have addressed these limitations by designing asymmetric samples that produce large-scale magnetic fields on a corroding sample, which would be capable of reflecting corrosion activity.

2. Experimental Section

2.1. SQUID Facility at Vanderbilt University. The high-resolution SQUID magnetometer facility is located in an experimental area with low magnetic gradients, provided by a specially designed iron-free vault built underground adjacent to the laboratory space but outside the main structure of the Physics building.

The custom-built SQUID magnetometer operating in liquid helium (Tristan Technologies, Inc.) has a three-axis vector gradiometer system with a noise-canceling reference SQUID. For each axis, a first-order differential gradiometer uses a pair of pickup coils (∅ 3 mm) separated vertically by a 30 mm baseline. The minimum operational distance between the z pickup coil and the room-temperature region outside the dewar is 2.5 mm. The SQUID is controlled by modified QD 5000 (Quantum Design) electronics that provide external feedback on four channels.

A magnetic shield with dimensions of 1 m × 1.7 m × 2 m consisting of two layers of Amumetal and two layers of aluminum provides an environment for the SQUID with magnetic fields less than 12 fT/Hz$^{-1/2}$.[40] A nonmagnetic, high-speed $x-y$ scanning stage driven by two stepper motors was placed outside of the magnetic shield. It provides repeatable scans with positioning accuracy of approximately 0.1 mm.

2.2. Experimental Set Up and Corrosion Cell Design. The experimental setup of the magnetic imaging system consisted of the three-axis differential magnetometer, magnetic shield, $x-y$ stage, and SQUID and motor control electronics (Figure 1). The experiment configuration enabled electrolyte supply to the corrosion cell in the magnetic shield as well as gas supply to the electrolyte reservoir. The solution was either deoxygenated by nitrogen or oxygenated by oxygen gas bubbling in the electrolyte reservoir.

Figure 2 shows the corrosion cell design as well as the geometry of the samples used. The U-shaped samples were prepared from a commercial 1.5 mm thick AA 2024 aluminum alloy plate (McMaster Carr). Three different sample configurations were used, which are described as asymmetric (A), symmetric (B), and asymmetric-sectional (C, Figure 2). The samples were glued on to a plastic cover using epoxy resin and
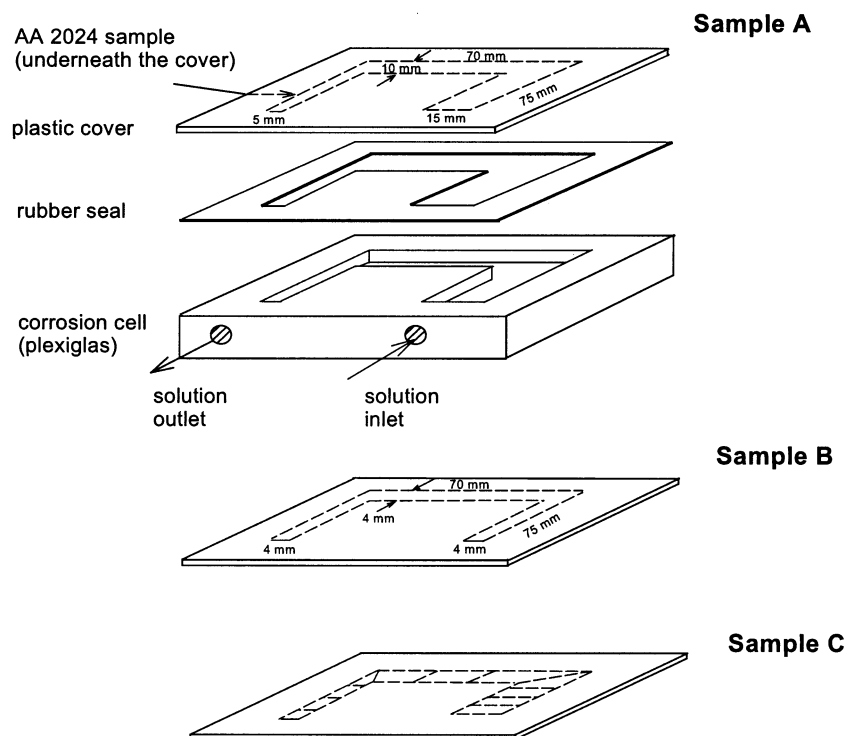
Figure 2. Corrosion cell with the AA 2024 samples (A, B, and C) underneath the cover used in the SQUID magnetometry experiments. Sample dimensions are indicated on the drawing.

all sides of the sample were isolated by the resin. The intersectional gaps of the sample C were filled with resin as well. The corrosion cell was assembled as depicted in Figure 2 using eight plastic screws (not shown). The solution was supplied to the cell via plastic tubes (Nalgene Premium Tubing, $^{1}/_{4}$).

2.3. SQUID Measurements. The sample surface treatment before each experiment included sandpapering (grade 320 and 600), cleaning with filter paper, rinsing with acetone, drying under ambient conditions, washing with distilled water, and drying again.

The distance between the SQUID dewar and the metal/solution interface was ca. 5.5 mm, which included the air gap between the dewar and the corrosion cell surface (2 mm), the cell cover thickness (2 mm), and the thickness of the sample (1.5 mm).

First, a background magnetic field image (BG) was obtained by scanning the dry sample. Then, solution was introduced to the sample and the magnetic image of the corroding surface was obtained (BC). The SQUID data were processed by using a special program, which subtracts one image from another and calculates the spatially integrated magnetic activity (SIMA, for definition see the discussion section and refs 8 and 10). The images given throughout the paper are the magnetic flux densities measured over the area of the z-axis pickup-coil of the magnetometer (B_z) and are presented as a difference $B_z =$ BC − BG.

2.4. EQCM, Alloy Deposition on Quartz by Magnetron Sputtering. The influence of oxygen on aluminum alloy corrosion was studied in situ by using an electrochemical quartz crystal microbalance (EQCM), which is a sensitive mass change detector with resolution of 10^{-9} g cm^{-2}. Quartz disks (AT plane) were used, their fundamental frequency being $f_0 = 5$ MHz and $d = 15$ mm (KVG Quartz Crystal Technology GmbH, Germany). The aluminum alloy was deposited on the quartz

substrates by DC magnetron sputtering (MS) using AA 2024 alloy as a sputtering target. The vacuum in the magnetron-sputtering chamber was maintained at 0.1−0.2 Pa using Ar as the working gas. The temperature in the chamber was ca. 50 °C. The Ar ionization current was 60 mA and the voltage was 450 V. The sputtering duration was 10 min, which corresponded to a coating thickness of ca. 0.2−0.3 μm. More details about the MS procedure and properties of deposits are given elsewhere.[41−43]

Both quartz sides were plated; the coatings acted as excitation electrodes in the oscillation circuit. The specimens were mounted as a window of a Teflon cell, with one of the sides being exposed to the solution compartment and the other one facing air. The actual electrode area in contact with the solution was 0.78 cm^2. The EQCM experimental device allowed the frequency to be measured at 0.01s intervals with a resolution of 0.1 Hz. The proportionality coefficient between the frequency and the mass change according to Sauerbrey's equation[44] was $C = 18$ ng Hz^{-1} cm^{-2} at $f_0 = 5$ MHz. The EQCM measurements were started several seconds after the cell had been filled with the solution.

3. Results and Discussion

3.1. Influence of Oxygen on AA 2024 Corrosion. A search for a correlation between corrosion and magnetic activity requires that SQUID measurements are performed at different corrosion rates. One way to govern corrosion rate is to control oxygen concentration. This is straightforward technically, and the corrosion process due to oxygen reduction is not complicated by gas evolution

$$O_2 + 2H_2O + 4e \rightarrow 4OH^- \quad (E° = 0.816 \text{ V}_{H/H+} \text{ at pH 7)} \quad (1)$$
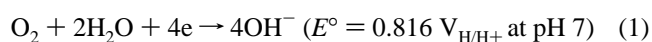
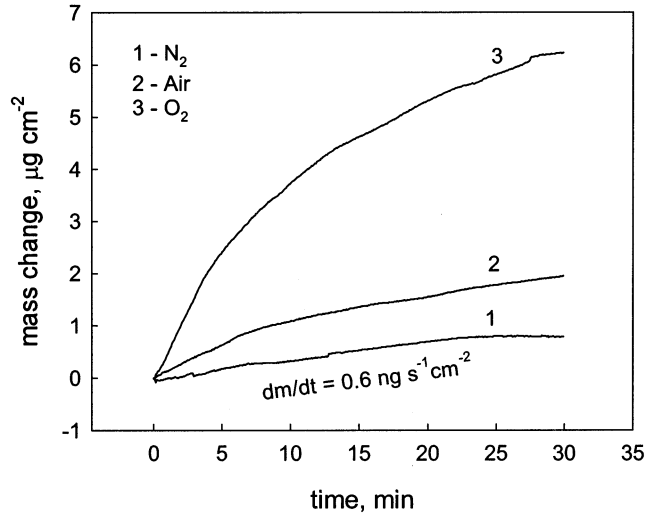It is commonly known that aluminum corrodes because of the

Figure 3. Mass change vs time obtained by electrochemical quartz crystal microbalance (EQCM) for magnetron-sputtered Al–Cu–Mg coating on quartz substrate (for composition see Table 1) in oxygen-free (1), naturally aerated (2), and oxygen saturated (3) 3.5% NaCl solution.

TABLE 1: Composition of the Alloy Deposited by Magnetron-sputtering (MS) Using AA 2024 as a Target on Quartz Substrates[a]

sputtering time	Al	Mg	Cu	Fe	Mn	O
0	60.57	1.15	2.20	0.36	0	35.72
30	72.92	1.08	2.19	0.20	0.28	23.33
60	80.07	0.75	3.64	0.26	0.57	14.69
120	83.87	0.69	4.48	0.78	0.90	9.27

[a] The data (in mass %) were obtained by X-ray photoelectron spectroscopy (XPS) using surface etching by ionized argon.

TABLE 2: AA 2024 Composition Used as a MS Target Determined by XPS and Surface Etching by Ionized Argon

sputtering time	Al	Mg	Cu	Fe	Mn	O
120	75.28	0.63	5.86	0.41	0	17.81
240	77.56	0.86	4.67	0.44	0	16.47

water decomposition reaction[45]

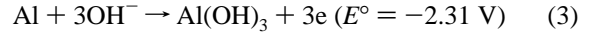$$2H_2O + 2e \rightarrow H_2 + 2OH^- \ (E° = -0.413 \ V_{H/H+} \text{ at pH 7}) \tag{2}$$
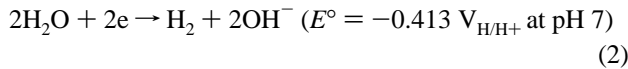
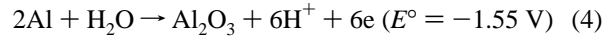The question, therefore, arises how significantly oxygen may affect AA 2024 corrosion.

The influence of oxygen on the corrosion process was determined by EQCM measurements (Figure 3). The XPS analysis showed that the sputtered films used for EQCM measurements had a similar content of elements in comparison to the bulk alloy used as a sputtering target (Tables 1 and 2). It should be noted that, because of some differences in the structure, sputtered and casting alloys could differ in their resistance to corrosion as was discussed in detail previously.[41–43,46] However, this aspect was beyond the scope of the present investigation, because the sputtered specimens were used to characterize corrosivity of the media, i.e., the oxygen effect on the alloy corrosion.

Figure 3 shows mass change dynamics obtained by EQCM after specimen immersion in the oxygen-free 3.5% NaCl solution as well as in equilibrium with air and oxygen. The general EQCM response in the oxygen-free solution is mass gain, which

implies accumulation of corrosion products on the corroding surface

$$Al + 3OH^- \rightarrow Al(OH)_3 + 3e \ (E° = -2.31 \ V) \tag{3}$$

or/and

$$2Al + H_2O \rightarrow Al_2O_3 + 6H^+ + 6e \ (E° = -1.55 \ V) \tag{4}$$

The mass gain rate (dm/dt) can be converted to corrosion current density (j_{corr}, A cm^{-2}) according to Faraday's law

$$j_{corr} = \frac{nF}{\Delta M} \frac{dm}{dt} \tag{5}$$

where F is the Faraday constant, n is the number of electrons in the corrosion reaction, and ΔM is the molar mass of the group responsible for the mass gain during corrosion (O, OH, OOH, H$_2$O, etc.). From the average slope $dm/dt = 0.6$ ng s^{-1} cm^{-2} in the deoxygenated solution (Figure 3), we found a corrosion current density as high as $j_{corr} = 3.38 \ \mu A \ cm^{-2}$, assuming hydrargillite (Al$_2$O$_3 \cdot 3$H$_2$O) as a most probable corrosion product.[47] The corrosion in the oxygen-free solution (N$_2$ atmosphere) could be ascribed to water decomposition (2) or free proton reduction

$$2H^+ + 2e \rightarrow H_2 \ (E° = 0.0 \ V_{H/H+}) \tag{6}$$
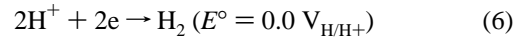
Obviously, oxygen affects the mass gain, i.e., the corrosion rate (Figure 3). A rapid mass growth in the oxygen-saturated solution indicates much higher corrosion activity than that observed in the naturally aerated solution. Accordingly, the corrosion rate in naturally aerated solution is much higher when compared to the oxygen-free solution. The AA 2024 alloy corrosion mechanisms are discussed in detail elsewhere.[32–39]

Thus, the EQCM measurements revealed that AA 2024 corrosion is determined by two processes: water decomposition (proton reduction) and oxygen reduction. Because of the significant dependence of AA 2024 corrosion rate upon oxygen concentration, variation of the latter provides a mechanism by which we can to control corrosion processes in SQUID experiments.

3.2. SQUID Measurements. Figure 4 shows magnetic flux images obtained over different samples corroded in 3.5% NaCl solution under natural aeration: asymmetric (A, Figures 2 and 4a), symmetric (B, Figures 2 and 4b), and asymmetric sectional (C, Figures 2 and 4c). Asymmetric samples A and C had equal surface areas ($S_A \approx 17$ cm^2); however, sample C consisted of eleven sections separated by 0.5 mm isolating gaps, which prevented electric current flow along the sample (Figure 2). All three sides of the asymmetric samples were of different width (4, 8, and 14 mm), whereas the symmetric sample had equal sides (4 mm, $S_B = 8.5$ cm^2).

The total magnetic activity of the corroding samples was estimated using the spatially integrated magnetic activity (SIMA, nT mm^2)[8,10]

$$SIMA(t_k, \Delta t) = \sum_i^{N_x} \sum_j^{N_y} [B_z(x_i, y_j, t_k, \Delta t)] \Delta x \Delta y \tag{7}$$

where B_z is the magnetic flux density measured over the z-axis pickup coil of the magnetometer and Δx and Δy represent the distance between two consecutive pixels in the corresponding scan direction. The SIMA calculation takes the summations over all of the pixels in the magnetic image, i.e., this value is
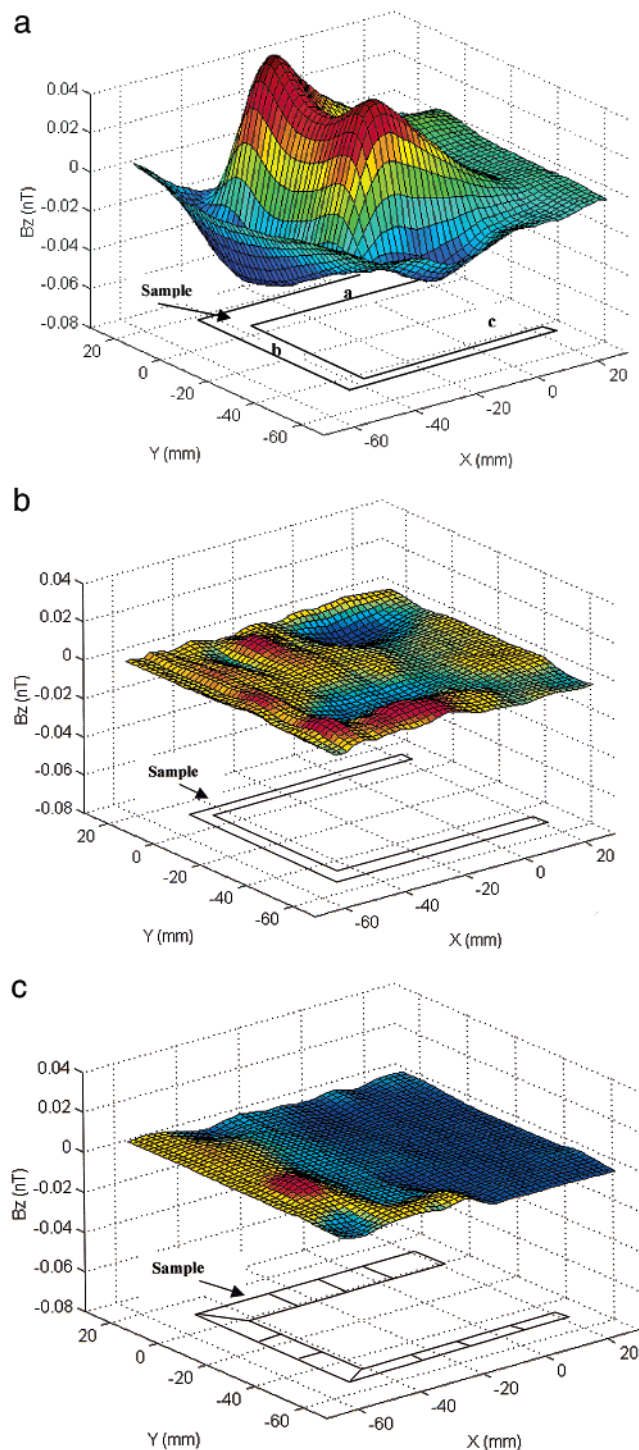
Aluminum Alloy Corrosion Sensing

J. Phys. Chem. B, Vol. 106, No. 48, 2002 **12553**

a

b

c

Figure 4. Magnetic field images obtained for the samples in Figure 2 in naturally aerated 3.5% NaCl solution: (a) asymmetric sample (Figure 2, *A*) $SIMA_A$ = 147 nT mm²; (b) symmetric sample (Figure 2, B) $SIMA_B$ = 34 nT mm²; (c) sectional sample (Figure 2, C) $SIMA_C$ = 28 nT mm².

proportional to the net magnetic activity of the sample during the surface scanning time.

The magnetic image in Figure 4c shows that sectional sample C is practically silent; no distinctive magnetic field zones are observed on the image. Sample B exhibits a somewhat higher magnetic activity and the field image bears a resemblance the sample configuration (Figure 4b). Asymmetric sample A shows the highest activity (Figure 4a). The magnetic field distribution over this sample reflects the geometry, with clearly pronounced activities at two edges.
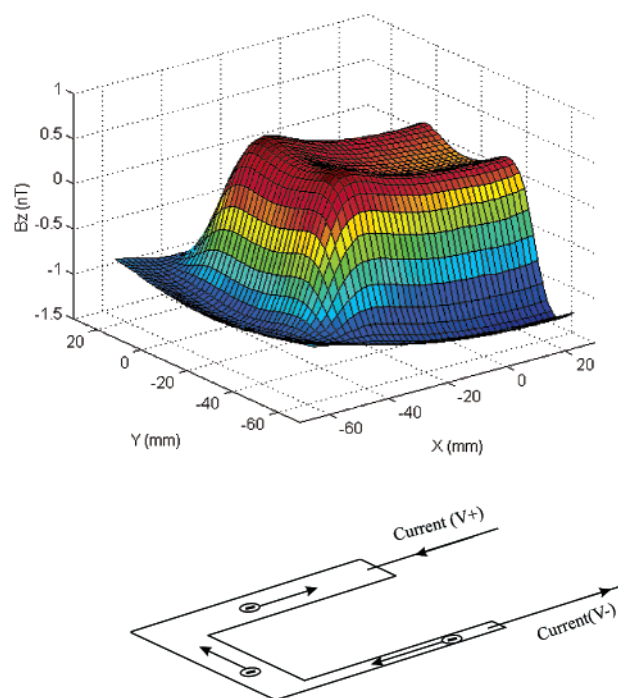

Figure 5. Magnetic field image obtained when a dc current (0.1 mA) was passed through sample A (Figure 2). The sample was mounted on the G-10 plate and the contacts were glued to the ends of the sample using silver paint. Current polarity is indicated on the figure, as is the direction of the electron motion.

The SIMA value was found to be as high as 147 nT cm² for sample A (Figure 4a), 34 nT cm² for sample B (Figure 4b), and 28 nT cm² for sample C (Figure 4c). Thus, the asymmetric sample A exhibited much higher magnetic activity than the two other samples.

Our results imply an electronic current flow along asymmetric sample A during the corrosion process (Figure 4a). The origin of the current lies in the appearance of an electromotive force because of corrosion potential (E_{corr}) gradient along the sample. It is commonly known that the corrosion potential may depend on electrode geometry because of different accessibility of the surface to corrosion agent and consequently different pH and solution chemical composition in the vicinity of corroding surface. It is difficult to predict the difference in E_{corr} on the basis of formal kinetics because the corrosion potential depends on a complex set of kinetic and thermodynamic factors, for instance, transport and reduction rate of oxidizers, equilibrium potential of metal and oxidizer, surface activity, etc. An experimental determination of the spatial distribution of E_{corr} within the corroding sample would require scanning electrochemical techniques using Kelvin microprobe or reference microelectrode, etc., which is yet not possible in a SQUID experiment. It is interesting to note that potential and current distribution across the corroding sample could be estimated by model calculations of magnetic fields by using Laplace's equation.[15] The author has calculated the potential gradient across a AA 7075-T6 disk corroding in a highly aggressive NaOH environment. The potential drop was found as high as a fraction of a nanovolts per centimeter.

The current flow along the corroding sample and its direction was also confirmed by an experiment in which an external dc current (0.1 mA) with the electron flow direction from the narrow side to the broad one was applied to the asymmetric sample (Figure 5). Obviously, the dc image corresponds to that of the corroding sample (Figure 4a), with the main difference

TABLE 3: Ratios between SIMA and Total Mass Changes during Corrosion (Δm_{corr}, $t = 20$ min) Calculated for Asymmetric Sample (A, Figure 2) in Nitrogen, Air, and Oxygen Atmospheres According to the Data in Figures 4a and 6, parts a and b

atmospheres	ratio between SIMA	ratio between Δm_{corr}
O_2/N_2	2.1	7.9
O_2/Air	1.6	3.4
Air/N_2	1.3	2.3

being that in Figure 5 the applied electron current flows to the end of the sample whereas in Figure 4 the corrosion current diminishes closer to the ends. Thus, the magnetic image of an applied current can serve as a diagnostic criterion to determine the direction of the current flow during the corrosion process, viz., the sign of ΔE_{corr} between different parts of electrode. The dc-current data (Figure 5) clearly indicate that the narrow side of the corroding sample (c, Figure 4a) has more a negative potential than the broad side (a), i.e., $E_{corr,c} < E_{corr,a}$. Consequently, anodic reactions 3 and 4 are more favored on side c, whereas cathodic reactions 1 and 2 are predominant on side a. This difference causes electron flow from side c to side a, whose magnetic component was registered in Figure 4a. In accordance, both sides of the symmetric sample are more or less equal, and therefore, magnetic activity of this sample was much less (Figure 4b). The current flow was prevented in sectional sample C by insulating gaps (Figure 4c), and consequently, this sample was magnetically almost silent (only small signals appear around the corners due to asymmetry of the individual sections).

The magnetic sensitivity of the asymmetric sample to corrosion was proven by the experiments in deoxygenated (Figure 6a), naturally aerated (Figure 4a), and oxygen-saturated (Figure 6b) solutions. As it was demonstrated above by EQCM experiments, the corrosion rate depends on oxygen concentration in the solution. It is seen that the magnetic activity responds to corrosion rate change, viz., the higher corrosion rate, the higher magnetic activity is observed: $SIMA_{N2} = 114$ nT mm^2 (Figure 6a), $SIMA_{AIR} = 147$ nT mm^2 (Figure 4a), and $SIMA_{O2} = 235$ nT mm^2 (Figure 6b).

The SIMA value represents a result of the summations of the magnetic activity within the scanning time, which was ca. 20 min in our experiments. A corresponding average corrosion activity is reflected by a total mass change because of corrosion (Δm_{corr}) registered by EQCM within the same time period (Figure 3). The ratios between SIMA and Δm_{corr} ($t = 20$ min) for different atmospheres are given in Table 3. The ratios for mass change are 2−3 times higher than those for SIMA. This implies that some part of the corrosion because of oxygen reduction remained magnetically silent. It should also be noted that corrosion because of oxygen reduction represents only a part of entire corrosion process. Another part is due to proton reduction (6) or water decomposition (2), whose magnetic activities are demonstrated in the oxygen-free solution (Figure 6a).

It is important that solution saturation by oxygen does not change the magnetic activity of the sectional sample (Figure 6c). The magnetic activity of this sample in the naturally aerated solution was $SIMA_{AIR} = 28$ nT mm^2 (Figure 4c) and the same value is observed in the oxygen-saturated solution (Figure 6c). Likewise as in air atmosphere, the sectional sample in oxygen atmosphere is characterized by the approximately 1 order of magnitude lower SIMA value when compared to its monolithic counterpart (Figure 6b). This indicates once again that the magnetic fields on the monolithic sample are induced mainly by a current flowing along the sample. Partial corrosion reactions
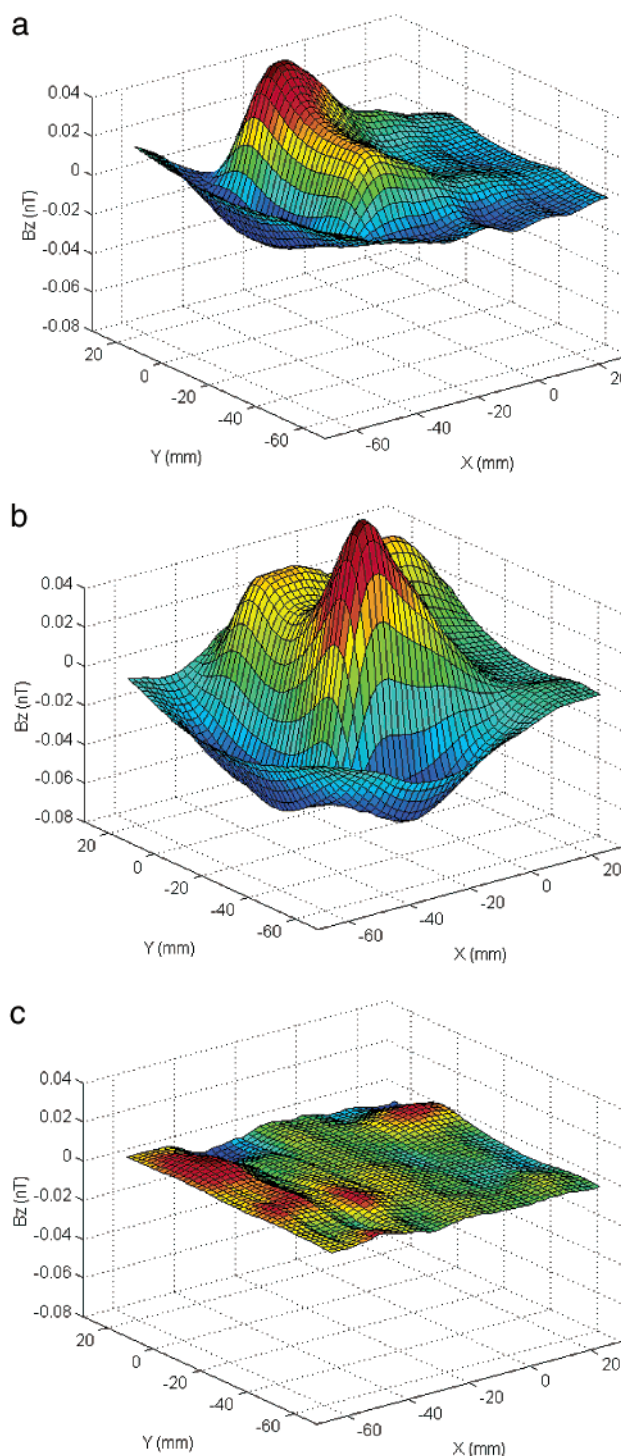
Figure 6. Magnetic field images with differing oxygen concentration: (a) asymmetric sample A (Figure 2) in deaerated 3.5% NaCl solution ($SIMA_A = 114$ nT mm^2); (b) the same sample in oxygen-saturated 3.5% NaCl solution ($SIMA_A = 235$ nT mm^2); (c) sectional sample C (Figure 2) in oxygen-saturated 3.5% NaCl solution ($SIMA_A = 28$ nT mm^2).

are the source of this current and the electromotive force emerges owing to corrosion potential gradient within the sample.

It is important to emphasize that a (*uniformly*) corroding surface may be magnetically silent on a macroscopic scale if no special measures are undertaken to induce any macroscopic nonequipotential zones on the surface. As it was demonstrated, the system that consisted of many single sections of different size and geometry (Figures 4c and 6c) responded magnetically to corrosion neither to air nor to oxygen atmosphere because

Aluminum Alloy Corrosion Sensing

J. Phys. Chem. B, Vol. 106, No. 48, 2002 **12555**

the electric potential gradient within each section is much smaller than that in Figure 4a.

In our sample geometry, the electronic currents in the aluminum alloy produce a magnetic field that is oppositely directed to that from the ionic currents flowing in the large volume of the bath beneath the sample. This contributes to a reduction in the strength of the observed magnetic field as compared to that produced by the electronic currents alone. The fact that the electronic and ionic currents flow in differently shaped volumes that are different distances from the SQUID prevents complete cancellation of the electronic magnetic field by the ionic one. These phenomena are of importance when developing SQUID corrosion sensing techniques for practical applications.

4. Conclusions

Macroscale magnetic fields were produced by corroding AA 2024 samples owing to their asymmetric geometry. The distinctive magnetic field images indicated an electronic current flow along the corroding sample, which originated from the corrosion potential gradient within the sample. The image of the corroding sample was qualitatively similar to that obtained from a dc current. The sample was magnetically sensitive to corrosion: a higher corrosion rate was associated with it a higher magnetic activity.

EQCM measurements in solutions with different oxygen concentration revealed that oxygen plays a significant part in aluminum alloy corrosion. Some part of the corrosion because of oxygen reduction remained magnetically silent. This was evident from the ratios between total mass change and integrated magnetic activity in argon, air, and oxygen atmospheres.

A sample comprising a system of single sections did not produce significant magnetic field while corroding in air-equilibrated and oxygen-saturated solutions; its magnetic activity was much less than that of the monolythic counterpart. These data indicated that the uniformly corroding surface could be magnetically silent on a macroscopic scale, if no special measures are undertaken to induce nonequipotential zones on the surface. The macroscopic electric potential gradient can be induced by broken symmetry of the corroding surface.

References and Notes

(1) Bellingham, J. G.; MacVicar, M. L. A.; Nisenoff, M.; Searson, P. C. *J. Electrochem. Soc.* **1986**, *133*, 1753.
(2) Bellingham, J. G.; MacVicar, M. L. A.; Nisenoff, M. *IEEE Trans. Magn.* **1987**, *23*, 477.
(3) Hibbs, A. D. *IEEE Trans. Magn.* **1992**, *139*, 2447.
(4) Hibbs, A. D.; Saeger, R. E.; Cox, D. W.; Aukerman, T. H.; Sage, T. A.; Landis, R. S. *Rev. Sci. Instrum.* **1992**, *63*, 3652.
(5) Li, D.; Ma, Y. P.; Flanagan, W. F.; Lichter, B. D.; Wikswo, J. P., Jr. *J. Miner. Metals Mater.* **1995**, *47*, 36.
(6) Li, D.; Ma, Y. P.; Flanagan, W. F.; Lichter, B. D.; Wikswo, J. P., Jr. *Corrosion* **1996**, *52*, 219.
(7) Li, D.; Ma, Y. P.; Flanagan, W. F.; Lichter, B. D.; Wikswo, J. P., Jr. *Corrosion* **1997**, *53*, 93.
(8) Skennerton, G.; Abedi, A.; Kelly, R. G.; Wikswo, J. P., Jr. *J. Corros. Sci. Eng.* **2000**, *3/2* (at http://www.cp.umist.ac.uk/JCSE/).
(9) Richter, H.; Knecht, A. *Materialprüfung* **1997**, *39*, 390.
(10) Abedi, A.; Fellenstein, J. J.; Lucas, A. J.; Wikswo, J. P., Jr. *Rev. Sci. Instrum.* **1999**, *70*, 4640.
(11) Andrieu, C.; Dalard, F.; Rameau, J. J.; Alcouffe, F.; Reboul, M. *J. Mater. Sci.* **1998**, *33*, 3177.
(12) Juzeliunas, E.; Hinken, J. H. *J. Electroanal. Chem.* **1999**, *477*, 171.
(13) Juzeliunas, E.; Samuleviciene, M.; Sudavicius, A.; Hinken, J. H. *Electrochem. Solid State Lett.* **2000**, *3*, 24.
(14) Juzeliunas, E.; Hinken, J. H. *Electrochim. Acta* **2000**, *45*, 3453.
(15) Abedi, A. Ph.D. Thesis, Vanderbilt University, Nashville, TN, 2000.
(16) Murphy, J. C.; Hartong, G.; Cohn, R. F.; Moran, P. J.; Bundy, K.; Scully, J. R. *J. Electrochem. Soc.* **1988**, *135*, 310.
(17) Asanuma, M.; Aogaki, R. *J. Chem. Phys.* **1997**, *106*, 9930.
(18) Shannon, J. C.; Gu, Z. H.; Fahidy, T. Z. *J. Electrochem. Soc.* **1997**, *144*, L314.
(19) Lee, J.; Ragsdale, S. R.; Gao, X.; White, H. S. *J. Electroanal. Chem.* **1997**, *422*, 169.
(20) O'Brien, R. N.; Santhanam, K. S. V. *J. Appl. Electrochem.* **1997**, *27*, 573.
(21) Noninski, V. *Electrochim. Acta* **1997**, *42*, 251.
(22) Leventis, N.; Chen, M.; Gao, X.; Canalas, M.; Zhang, P. *J. Phys. Chem. B* **1998**, *102*, 3512.
(23) Hinds, G.; Coey, J. M. D.; Lyons, M. E. G. *J. Appl. Phys.* **1998**, *83*, 6447.
(24) Devos, O.; Olivier, A.; Chopart, J.; Aaboudi, O.; Maurin, G. *J. Electrochem. Soc.* **1998**, *145*, 401.
(25) Nakabayashi, S.; Kratsev, I.; Aogaki, R.; Inokuma, K. *Chem. Phys. Lett.* **1998**, *294*, 204.
(26) Grant, K. M.; Hemmert, J. W.; White, H. S. *Electrochem. Commun.* **1999**, *1*, 319.
(27) Waskaas, M.; Kharkats, Y. I. *J. Phys. Chem. B* **1999**, *103*, 4876.
(28) Shinohara, K.; Aogaki, R. *Electrochemistry* **1999**, *67*, 1261.
(29) Coey, J. M. D.; Hinds, G.; Lyons, M. E. G. *Europhys. Lett.* **1999**, *47*, 267.
(30) Hinds, G.; Spada, F. E.; Coey, J. M. D.; Ni Mhiochain, T. R.; Lyons, M. E. G. *J. Phys. Chem. B* **2001**, *105*, 9487.
(31) Rucinskiene, A.; Bikulcius, G.; Gudaviciute, L.; Juzeliunas, E. *Electrochem. Commun.* **2002**, *4/1*, 86.
(32) Wit, J. H. W. *Electrochim. Acta* **2001**, *46*, 3641.
(33) Chen, G. S.; Gao, M.; Wei, R. P. *Corros. Sci.* **1996**, *52*, 8.
(34) Wei, R. P.; Liao, C. M.; Gao, M. *Metall. Mater. Trans. A* **1998**, *29*, 1153.
(35) Buchheit, R. G.; Grant, R. P.; Hlava, P. F.; Mckenzie, B.; Zender, G. L. *J. Electrochem. Soc.* **1997**, *144*, 2621.
(36) Blanc, C.; Lavelle, B.; Mankowski, G. *Corros. Sci.* **1997**, *39*, 495.
(37) Guillaumin, V.; Mankowski, G. *Corros. Sci.* **1999**, *41*, 421.
(38) Liao, C.-M.; Olive, J. M.; Gao, M.; Wei, R. P. *Corrosion* **1998**, *45*, 451.
(39) Schmutz, P.; Frankel, G. S. *J. Electrochem. Soc.* **1998**, *145*, 2285.
(40) Ma, Y. P.; Wikswo, J. P., Jr. *Rev. Sci. Instrum.* **1991**, *62*, 2654.
(41) Leinartas, K.; Samuleviciene, M.; Bagdonas, A.; Sudavicius, A.; Lisauskas, V.; Juzeliunas, E. *Electrochem. Commun.* **2001**, *3*, 494.
(42) Leinartas, K.; Miecinskas, P.; Sudavicius, A.; Jelinskiene, D.; Juskenas, R.; Lisauskas, V.; Vengalis, B.; Juzeliunas, E. *J. Appl. Electrochem.* **2001**, *31* (10), 1079.
(43) Juzeliunas, E.; Leinartas, K.; Samuleviciene, M.; Sudavicius, A.; Miecinskas, P.; Juskenas, R.; Lisauskas, V. *J. Solid State Electrochem.* **2002**, *6*, 302.
(44) Sauerbrey, G. Z. *Z. Phys.* **1959**, *155*, 206.
(45) Kaesche, H. *Die Korrosion der Metalle*; Springer: Berlin, 1990.
(46) Juzeliunas, E.; Leinartas, K.; Samuleviciene, M.; Miecinskas, P.; Juskenas, R.; Sudavicius, A. *Corros. Sci.* **2002**, *44*, 1545.
(47) Pourbaix, M. *Atlas of Electrochemical Equilibria in Aqueous Solutions*; NACE: Houston, TX, 1974.